Cen, H., Nunez-Sanchez, S., Bickerton, I., Fox, N. A., & Cryan, M. J. (2020). Solar Thermal Characterisation of Micro-Patterned High Temperature Selective Surfaces. *Journal of Photonics for Energy, 10*(2), [024503]. https://doi.org/10.1117/1.JPE.10.024503

Solar Thermal Characterisation of Micro-Patterned High Temperature Selective Surfaces

H. Cen[1], S. Nunez-Sanchez[2], A.Sarua[3], I.Bickerton[3], N.A. Fox[3] and M.J.Cryan[1] *

[1]University of Bristol, Department of Electrical and Electronic Engineering, Bristol, BS8 1UB, UK

[2]University of Vigo, Department of Physical Chemistry & CINBO, Vigo, 36310, Spain

[3]University of Bristol, School of Physics, Bristol, BS8 1TL, UK

Abstract

This paper presents measured optical absorptivity, emissivity and maximum solar-heated temperatures for micro-patterned molybdenum. The molybdenum samples were fabricated using laser micromachining and characterised using an integrating sphere and an infrared microscope. In-air solar simulator-heated temperature results for the molybdenum samples with different microstructures are presented and COMSOL modelling is then used to predict in-vacuum maximum temperatures. A vacuum chamber was developed to reduce the convection heat loss with a mount designed to minimise conduction loss and a maximum measured temperature of 413 ℃ was obtained.

Keywords: solar, energy, absorption, heat transfer, molybdenum, micro-patterned

*M.J.Cryan, E-mail: m.cryan@bristol.ac.uk

1. Introduction

Solar thermal [1] energy converters have been widely studied for many years and are suitable for both small and large-scale deployment. Solar thermionic energy converters [2,25] are a much more direct and potentially more efficient way of generating electricity from solar energy. A basic thermionic converter consists of a hot cathode, which emits electrons which are collected by a cold anode, generating an electrical current. Compared to a conventional photovoltaic solar cell, solar thermionic converters are not restricted by the semiconductor band gap and can thus use more of the available solar energy. They are a type of Carnot engine and thus the upper limit of their efficiency is determined mainly by the difference between the hot and cold

temperatures and is equal to 58.2% for 500 ℃ and 50 ℃. A key feature of solar energy converters is the use of selective surfaces which aim to maximise solar absorption while minimizing infra-red emissivity in order to achieve the highest possible temperature. Much work has been done developing such surfaces, but they tend to be for lower temperatures < 300 ℃ [3, 4]. For thermionic emission [5,23] temperatures > 500 ℃ are required and this paper explores approaches to achieve such high temperature selective surfaces.

Recently, a number of low cost, micro and nanopatterning techniques such as laser etching [6], displacement Talbot lithography [7], electron beam lithography [8], nano-imprint lithography [9] and laser interference lithography [10] have been developed. This has enabled an number of new types of selective surface to be developed in order to improve solar absorption and reduce thermal emission of radiation in order to increase the conversion efficiency [11-16]. This paper studies the use of laser etching, which may not achieve optimum selectivity, but has the potential to be a low cost, large area technique. Molybdenum is used in particular because it is amenable to coating of high temperature thermionic materials such as nano-diamond [23]. This paper characterises the increased solar absorption and measures the reflectivity and subsequent temperature rise achieved using a solar simulator both in-air and under vacuum conditions.

2. Fabrication

Laser micromachining techniques including etching, drilling as well as cutting are widely used in various industrial applications [17, 18]. Here, we use a nanosecond pulsed Nd:YAG laser (ALPHA 532-XYZ-A-U system, Oxford Lasers) which operates at 532nm wavelength. Nine 1 cm x 1cm samples have been fabricated with 2D disordered periodic surface structuring with different average periods (10, 20 and 30 μm). The period is disordered due the nature of the laser pulsing and movement. The surfaces were made by single pulse laser firing at different laser energies (20%= 28.6 μJ/pulse, 30%= 38.3 μJ/pulse, 40%= 48.1 μJ/pulse) and Table 1 summarises the different samples. Each laser pulse ablates a certain amount molybdenum depending on the laser pulse energy, therefore the morphology of the holes depends on the pulse energy. As the energy per pulse increases the diameter and depth of laser ablated hole increases. The holes obtained at 28.6 μJ/pulse (smallest energy used) have a diameter around 20 μm (see Fig 1). The average period is controlled by the laser firing distance (see Fig. 2). All samples have been produced in large areas (1 cm^2) maintaining the patterning across the whole surface and allowing heating measurements under illumination. In order to maintain a flat surface the substrates were laser cut from a large molybdenum sheet (0.25 mm thickness, 1 kHz, 456 μJ/pulse, speed 1mm/s, 300 passes per line).

Table 1 Laser pulse period and laser energy used for 9 molybdenum samples

Sample Number	Pattern period [μm]	Laser energy [μJ/pulse]	Laser energy Percentage
1	10	28.6	20%

2	20	28.6	20%
3	30	28.6	20%
4	10	38.3	30%
5	20	38.3	30%
6	30	38.3	30%
7	10	48.1	40%
8	20	48.1	40%
9	30	48.1	40%

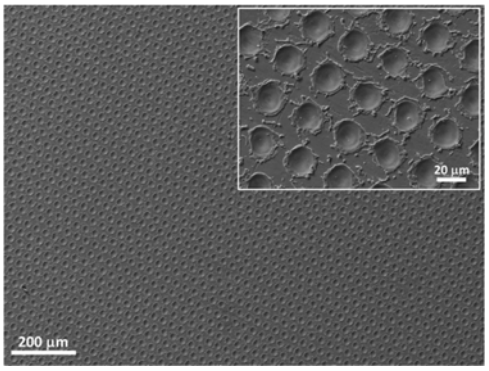

Figure 1 : SEM image of a laser patterned molybdenum sample produced at 20% laser power and 30µm period.

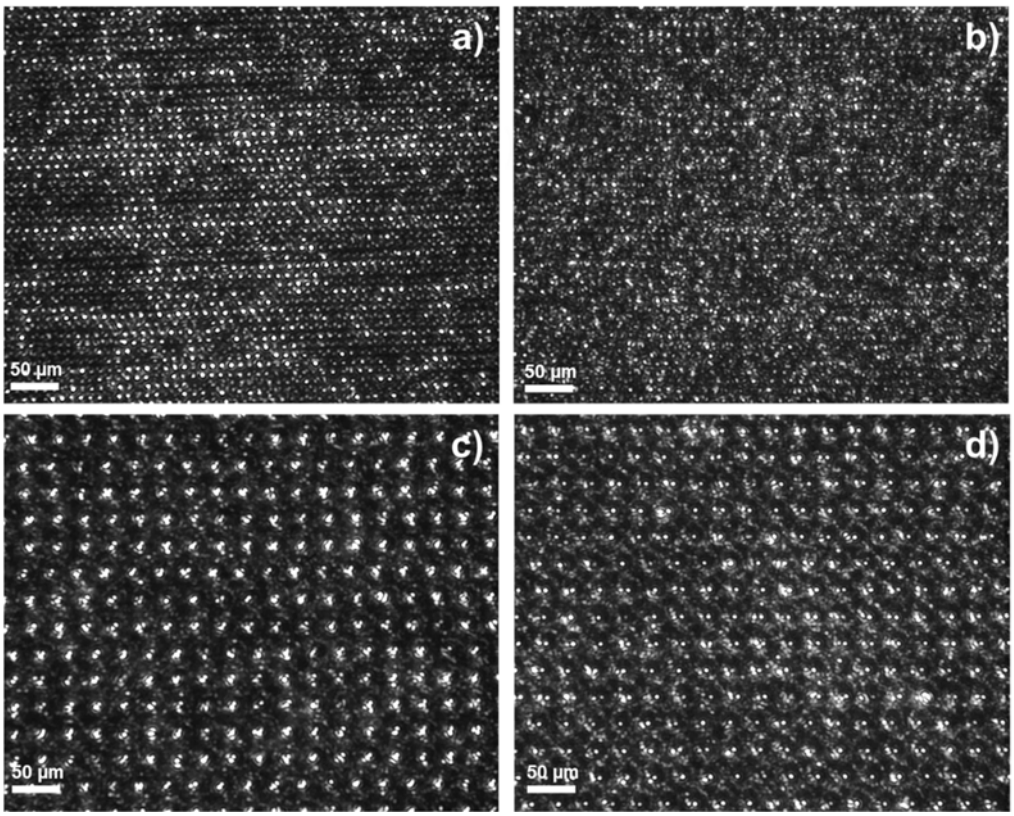

Figure 2 : Optical microscope images of the laser micro-patterned molybdenum surfaces at: a) 28.6 µJ/pulse and b) 48.1 µJ/pulse with a laser firing distance of 10µm, c) 38.3 µJ/pulse and d) 48.1 µJ/pulse with a laser firing distance of 30 µm.

3. Optical Characterisation

The reflectivity and absorptivity measurements were obtained using an Ocean Optics ISP-REF integrating sphere and an Ocean Optics USB2000+ spectrometer. As shown in Fig 3, the integrating sphere and the spectrometer were connected with an optical fibre. The integrating sphere was set to include both specular and diffuse reflections. We used an STAN-SSH high specular mirror as a reflectance standard.

Figure 3 : Optical measurement setup, an Ocean Optics ISP-REF integrating sphere on the right connected to an Ocean Optics USB2000+ spectrometer on the left.

The thickness of the molybdenum sheet is 0.25 mm therefore we can assume that the transmissivity (T) of the molybdenum samples is 0. According to the relation $R + A + T = 1$, where R is the reflectivity A is the absorptivity, we can thus calculate the absorptivity from $A = 1 - R$.

Fig 4 (a) shows the absorptivity from 500 to 900 nm of samples with the larger distance between holes (30 μm) produced at different laser energy per pulse. All the patterned samples shown a larger absorptivity in the visible range than the flat molybdenum. Moreover, we can observe that the absorptivity in all the wavelength range increases with the laser energy while the quasi-period is maintained. Therefore, the optical response is going to be directly related with morphology of the laser drilled holes, and we see that the absorptivity increases as the diameter and depth of the holes increase. On the other hand, the periodicity of the patterned surface only seems affect to the samples patterned with lowest energy per pulse (Fig. 4(b)) with variations between 40% and a 60%. However, in the case of samples patterned at highest laser energy, the

absorptivity remains similar between samples with values close to 70% (Fig. 4 (c)). This reveals that size and depth of the hole are the main parameters which affect the absorptivity in the VIS-NIR while period only affects in the case of patterned samples with the smallest features. Fig. 5 summaries all the trend for comparison with later temperature results.

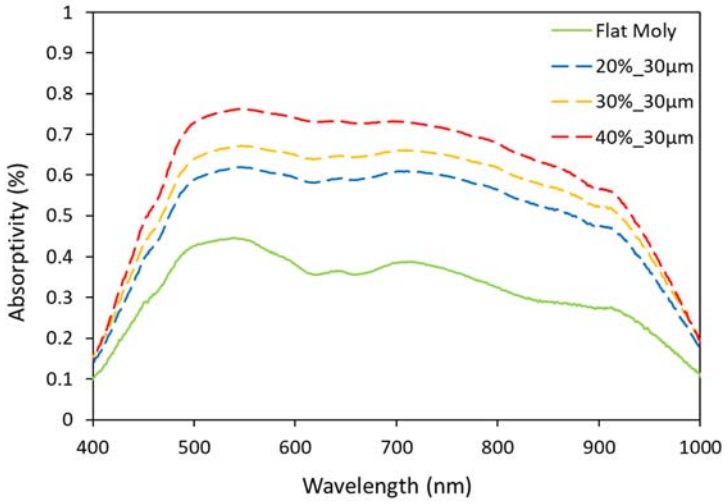

(a)

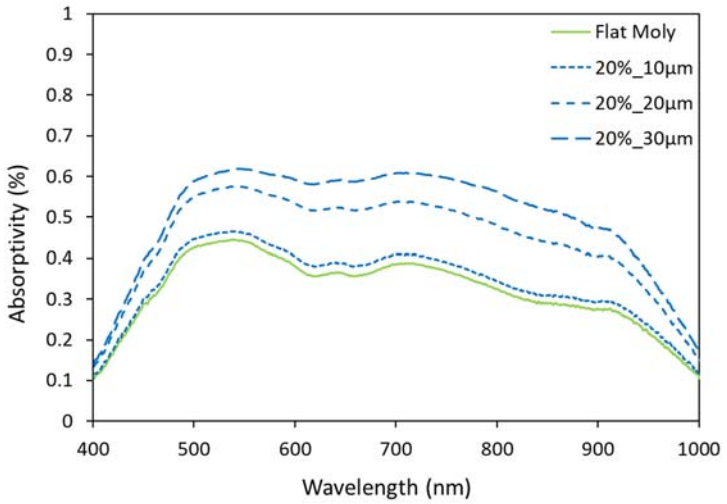

(b)

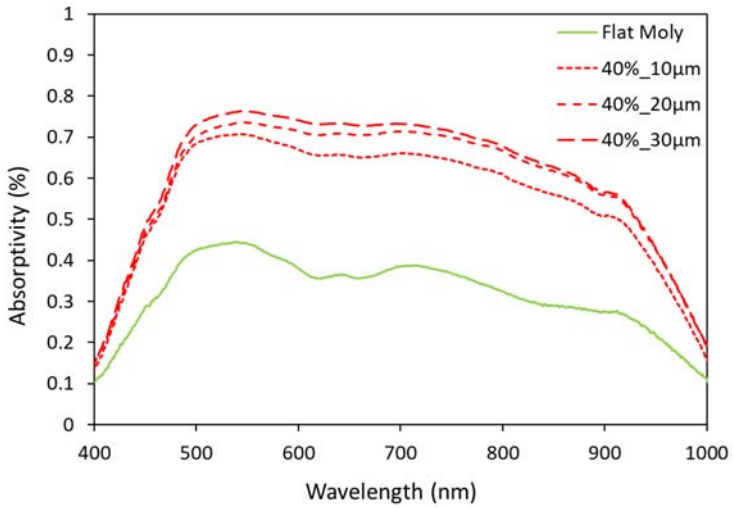

(c)

Figure 4 : Absorptivity of patterned molybdenum samples a) with an average period of 30 µm at three different laser energy per pulse, b) patterned at 28.6 µJ/pulse and c) 48.1 µJ/pulse with different average periods.

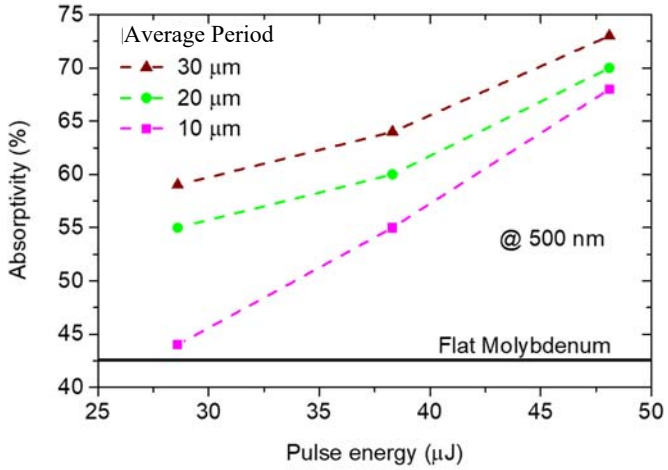

Figure **5 :** Absorptivity at 500 nm (wavelength at maximum of solar spectrum) for all samples as a function of the pulse energy and the average periods.

While the laser etching increased the absorptivity of the molybdenum samples over 500-900nm range, it is also important to investigate the emissivity at longer wavelengths. Our solar thermal applications operate at 800~1000K so the sample's emission mostly lies in 1.5-10µm. Here we measured the average surface emissivity of

three samples using a QFI Infrascope IR microscope instrument operating in the 2.5-5.5μm range with an InSb detector and a 15x IR lens. The samples were mounted on a Peltier heater and heated up to 75 deg C. Fig 6 shows the measured emissivity of both sides of sample 1, 5 and 6. We can see that the patterned surface of sample 6 has the highest emissivity of 0.35 and sample 1 has the lowest emissivity of 0.22. So larger and deeper holes on the sample surface also increase the total emissivity in the 2.5-5.5μm range.

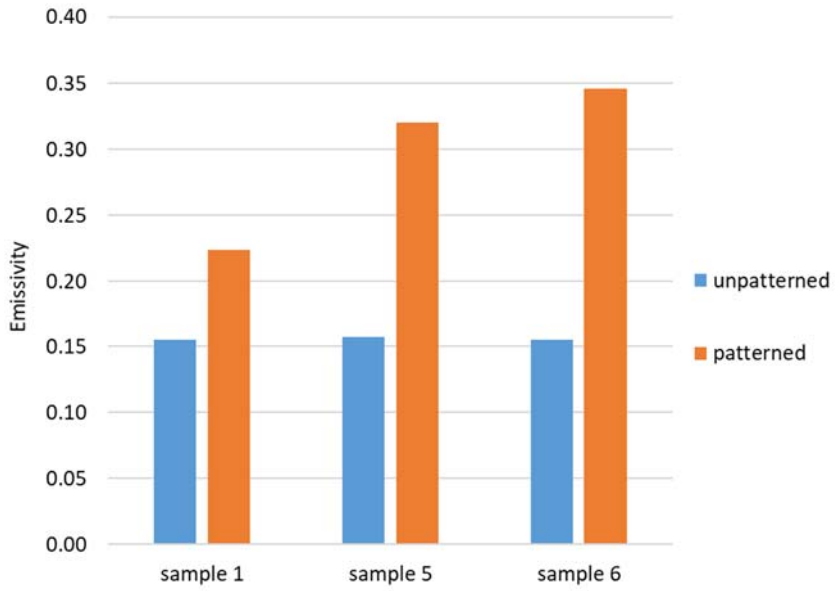

Figure 6 : Emissivity of both sides of sample 1, 5 and 6 at 75 ℃

4. Optical Simulation

Finite Difference Time Domain reflectivity simulations have been done with commercial Lumerical software with a planar light source and with and without periodic Bloch boundaries as shown in Fig. 7. Holes have been simulated as a trapezoids and molybdenum optical properties are from Palik[24]. Patterned surfaces

show larger values of absorptivity in the VIS-NIR wavelength range than flat molybdenum layer. Due to the period being much longer than the wavelength (solar spectrum) no differences between periodic and non-periodic boundaries have been observed revealing that the dominant parameter in the reflectivity response for large holes is mainly related with hole shape and size. We would like to remark that at maximum of the peak of solar spectrum (500 nm) the light is concentrated within the hole increasing the reflections at the molybdenum interfaces within the hole volume. Therefore, an increase of the temperature is expected due to the interaction of light with the walls of the hole.

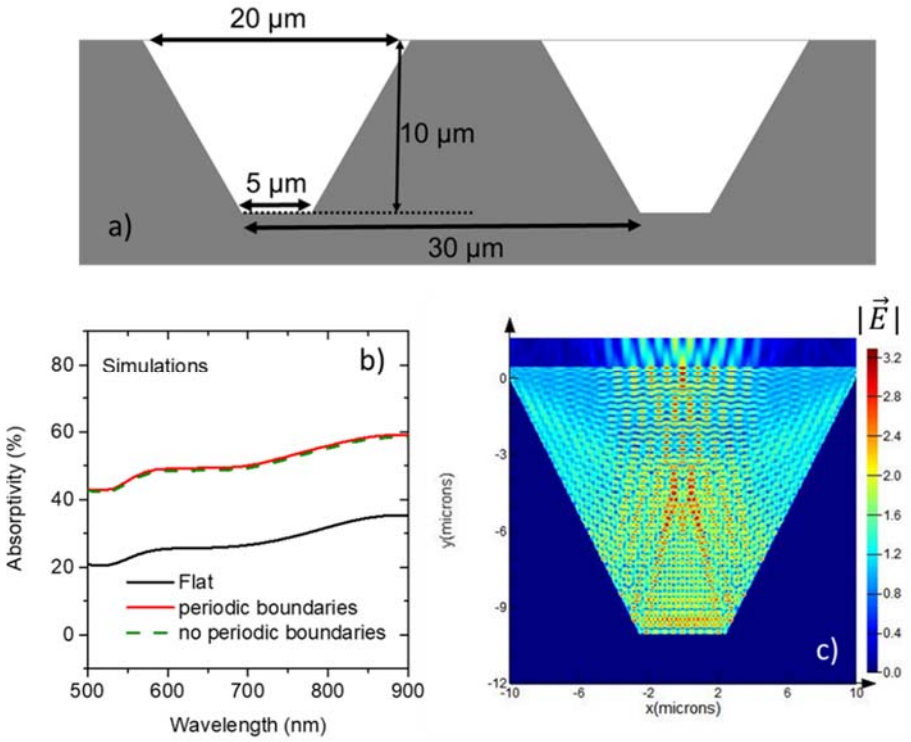

Figure 7 a) Simulated molybdenum periodic structure with trapezoidal holes. b) Absorptivity obtained from simulations of a flat molybdenum and a periodic and non periodic molybdenum structure. C) Electric field distribution inside the holes at 500 nm.

5. Thermal Results

Having done lower power optical characterisation the next stage was to characterise the temperatures that can be achieved under high power optical illumination. As shown in Fig 8 (a), samples were fixed on two glass slides and illuminated by a Newport Solar Simulator with an 100W Xenon arc lamp. To achieve more focused light, a spherical lens was used between the sample and the solar simulator. Temperature measurements were recorded over 500 seconds using a thermocouple attached to the back side of the samples.

Fig 8 (b) shows the highest temperatures reached by nine micro-patterned molybdenum samples and one flat molybdenum under 500s solar simulator illumination. We can see that the temperature measurements have good agreement with the absorptivity measurements at 500nm shown in Fig 5 and Sample 9 achieved the highest temperature due to its higher absorptivity in the 500-900 nm range.

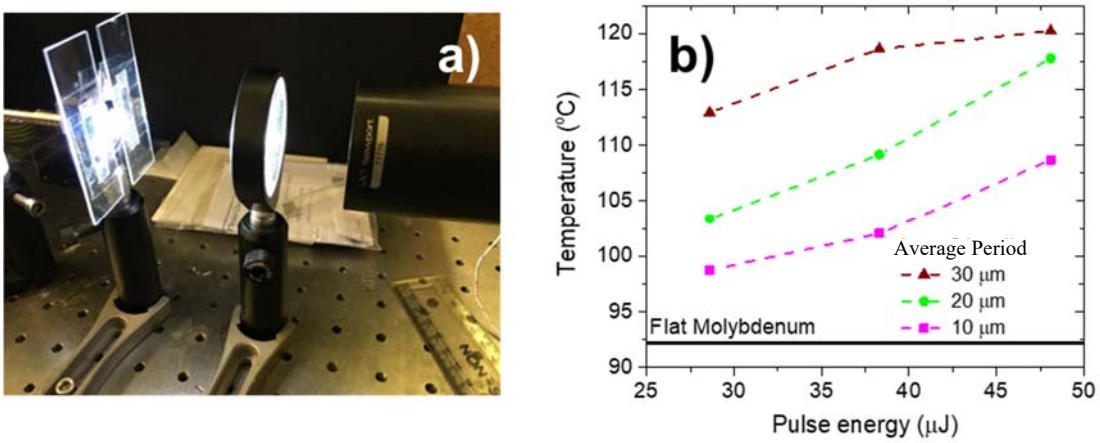

(a) (b)

Fig. 8 (a) Measurement setup. (b) Measurement of the highest temperatures reached by ten different samples under 500s solar simulator illumination. Flat molybdenum case is not dependent on pulse energy.

Vacuum device

For purpose of minimising the convection and conduction loss during the thermal experiments, we designed a vacuum device for mounting the samples as shown in Fig. 9. The sample is fixed on a round quartz holder with a cut-out in the centre. The conduction loss is minimised since quartz glass is an excellent thermal insulator. A K-type bare wire thermocouple is attached to the back side of the sample and its two ends connect to two copper tube terminals. The device is pumped into vacuum through one copper tube. We used one of the micro-patterned molybdenum samples (30 μm period and 30% laser energy Sample 6) and test both sides in air and vacuum. Before doing thermal testing we undertook thermal modelling using COMSOL.

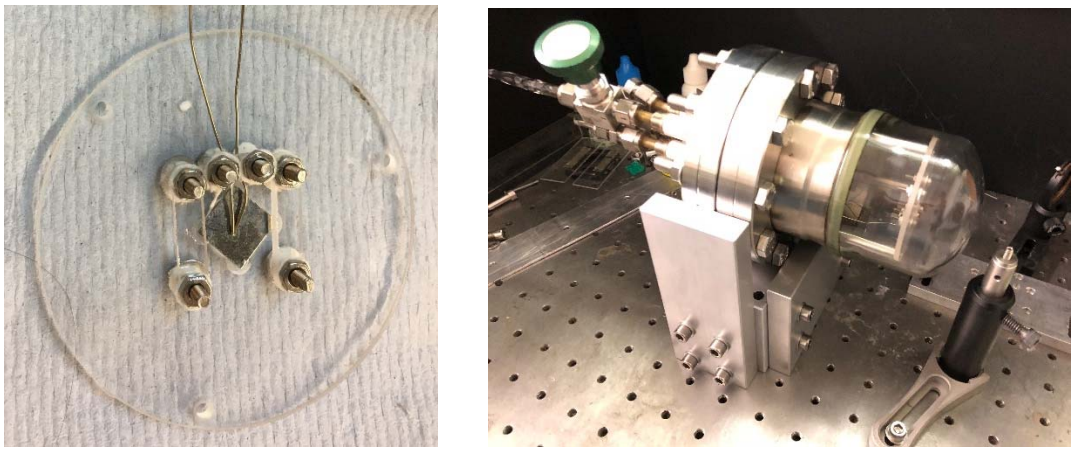

(a) (b)

Fig. 9 (a) Quartz holder for mounting the sample. (b) The vacuum device fixes on an aluminium base.

Thermal Modelling

COMSOL Multiphysics [19] is a powerful software platform for modelling physics-based problems. It is based on finite element method (FEM), which can solve partial differential equations in both 2D and 3D. In this paper, the Heat Transfer Module in

COMSOL Multiphysics is used to study the heating process of the metal surface and other objects connected to it. In the simulation, all mechanisms of heat transfer including conduction, convection and radiation can be modelled. The equation used to solve the heat transfer in solids is:

$$q = \frac{kA\Delta T}{l} \quad (1)$$

Where q is the heat transfer rate (W), k is the thermal conductivity $(W/(m \cdot K))$, A is the area of the object (m^2), ΔT is the temperature difference between air and surface (K) and l is the thickness of the object (m).

There are solid bodies in contact in our model. The heat transfer between the contacting surfaces can be solved using the equation:

$$q = \frac{\Delta T}{\frac{l_A}{k_A A} + \frac{1}{h_c A} + \frac{l_B}{k_B A}} \quad (2)$$

Where l_A and l_B are the thicknesses of solid A and solid B (m), k_A and k_B are the thermal conductivities of solid A and solid B $(W/(m \cdot K))$, h_c is the thermal contact conductance between solid A and solid B $(W/(m^2 \cdot K))$.

The experiment was conducted in air and the heat was transported by air due to natural heat convection. The thermal convection was modelled using the equation:

$$q = hA\Delta T \quad (3)$$

Where h is the convective heat transfer coefficient $(W/(m^2 \cdot K))$.

The convective heat transfer coefficient h is calculated through correlations provided by Churchill and Chu [20] and W.H.McAdams [21]. Three dimensionless

numbers, the Nusselt number Nu, the Rayleigh Number Ra and the Prandtl number Pr are used in the correlations. They can be derived from the following equations.

$$Nu = \frac{hL}{k} \quad (4)$$

$$Ra = \frac{\rho L^3 g \beta \Delta T}{\eta \alpha} \quad (5)$$

$$Pr = \frac{c_p \mu}{k} \quad (6)$$

Where L is the characteristic length, g is the acceleration due to gravity, β is the thermal expansion coefficient, η is the kinematic viscosity, α is the thermal diffusivity and μ is the dynamic viscosity.

In our model, we use the correlations of natural convection and external laminar flows for both vertical and horizontal plates. The equation for vertical plane is:

$$Nu = 0.68 + \frac{0.67Ra^{1/6}}{\left(1+(0.492/\mathrm{Pr})^{9/16}\right)^{4/9}} \quad (7)$$

For hotter surface facing up, the equation for horizontal plane is:

$$Nu = 0.14Ra^{1/3} \quad (8)$$

For hotter surface facing down, the equation for horizontal plane is:

$$Nu = 0.27Ra^{1/4} \quad (9)$$

From Eqs. 4-9, the convective heat transfer coefficients for each plane in the model are estimated and the convective heat loss can be calculated using Eq. 3.

The equation for calculating the radiation energy loss of an object is:

$$q = \sigma \varepsilon A\left({T_{amb}}^4 - {T_o}^4\right) \quad (10)$$

Where σ is the Stefan-Boltzmann constant, ε is the emissivity of the object, T_{amb} is the ambient temperature and T_o is the temperature of the object.

Fig 10 (a) shows the top view of the proposed quartz holder in COMSOL simulation. The diagonal cross section diagram is shown in Fig 11 The four corners of the molybdenum sample sit on the quartz holder which has a 11.8mm diameter round cut-out. The sample is heated by the solar source which can be modelled as a Gaussian distributed heat flux shown in Fig 10 (b) on the top surface of the sample. The temperature monitor is at the centre of the back surface of the sample. In the experiment, the molybdenum sample and the quartz holder are placed vertically as shown in Fig 9 (b). The recessed area of the quartz was rough due to the machining and the molybdenum sample was not pressed firmly onto the quartz. Therefore, the sample was not contacting with the quartz holder perfectly. This can result in reduced thermal contact conductance between the molybdenum sample and the quartz which means less thermal conduction from Eq. 2.

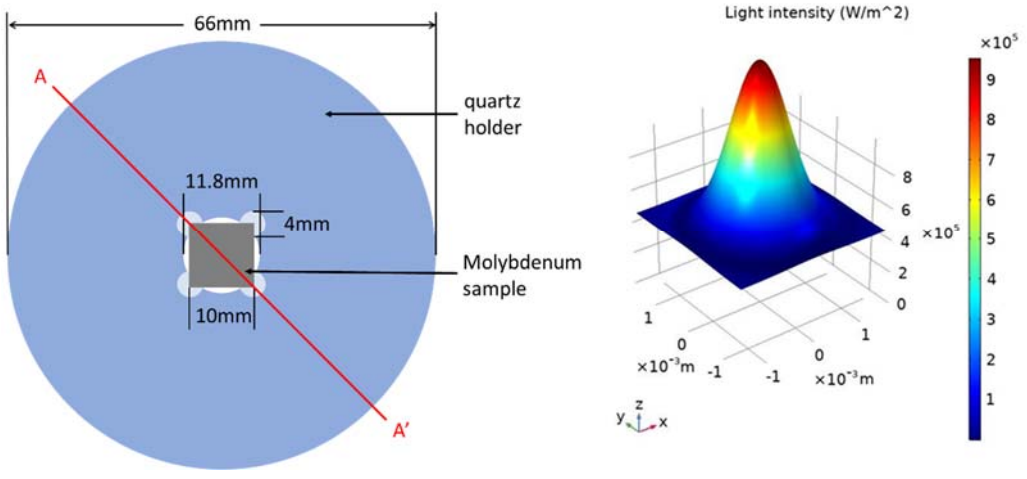

(a) (b)

Figure 10 **:** (a) Simulated top view of the proposed sample mounting mechanism with Molybdenum sample. (b) Example of a Gaussian profile heat source applied on top of the sample.

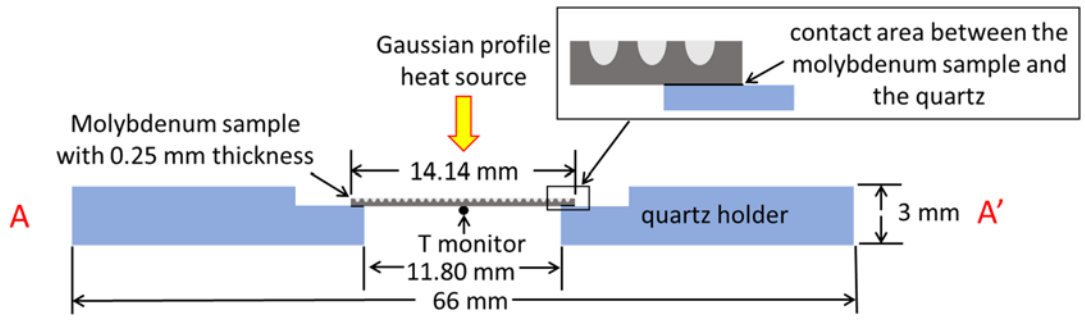

Figure 11 : Simulated cross section diagram of the proposed sample mounting mechanism with patterned surface on top

The simulations were for two molybdenum samples in three different cases as shown in Fig 12. Fig. 12(a) flat molybdenum with unpatterned surfaces. Figure 12(b) shows used patterned-flat, and Fig. 12(c) shows flat-patterned. We have chosen the simulation parameters to match with Sample 6, they are listed in Table 2. The measurement heat source will be the Newport 6255 Xenon Lamp with 67005 Arc Lamp Housing. According to the manual [22], the irradiance of the lamp is across 200-2400nm, so we divided the wavelength range into 3 sections and specified the power and the optical properties of the sample in different wavelength ranges. The solar simulator powers were calculated from the spectral irradiance of the lamp. The total output of the solar simulator is 4.4W and the total receiver area is 1 cm × 1 cm. We assume that 80% of the power is received by the sample through the lens and the glass window. Therefore, the radiant flux density on the sample is 3.5 x 10^4 W/m^2. From Fig 4, the absorptivity of patterned surfaces of sample 6 at 500-900nm was ~0.6 and the absorptivity of the unpatterned surface at 500-900nm was ~0.4. For 200-500nm and 900-2400nm wavelength, we assume the absorptivity of both patterned and unpatterned surfaces is 0.1. The emissivity of the patterned surface and the unpatterned surface are set to 0.35

and 0.16 from our previous measurements as shown in Fig. 6. The simulation includes six combinations: flat-flat, patterned-flat and flat-patterned in air and in vacuum. The convective heat transfer coefficients h in air for different planes are 5.4~44 $W/(m^2 \cdot K)$ which are derived from Eq. 3-8. In vacuum, we assume no convection occurs so h equals to 0 $W/(m^2 \cdot K)$. The illumination time was 1000s for both simulation and measurement which was enough for the samples to reach the highest temperature.

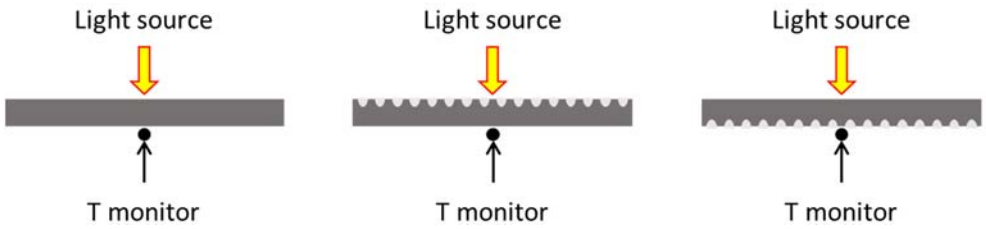

(a) (b) (c)

Figure 12 : Illustrations of three cases for the temperature measurements: (a) flat-flat, (b) patterned-flat and (c) flat-patterned.

Table 2 Parameters used in Comsol Multiphysics simulation

wavelength (nm)	**200-500**	**500-900**	**900-2400**	**2500-5500**
solar simulator power (W)	0.8	1.5	2.1	-
absorptivity of patterned molybdenum	0.1	0.6	0.1	-
absorptivity of unpatterned molybdenum	0.1	0.4	0.1	-
emissivity of patterned molybdenum	-	-	-	0.35
emissivity of unpatterned molybdenum	-	-	-	0.16

Fig. 13 summarises the simulation results of the effects on the highest achieved temperatures of varying the thermal contact conductance between the molybdenum sample and the quartz in six combinations. It can be seen that the samples achieved higher temperatures in vacuum than in air due to much less thermal convection. It

clearly shows that increasing the thermal contact conductance increases the conduction loss from the sample to the quartz, which leads to lower temperature. It also shows that the patterned-flat case obtains the highest temperature when the thermal contact conductance is more than $100\ W/(m^2 \cdot K)$. This is because the patterned-flat case has higher absorption than the other two cases. However, when the thermal contact conductance is less than $100\ W/(m^2 \cdot K)$ the flat-flat case achieves a higher temperature than the patterned-flat and this seems somewhat unexpected. However, there are a number of effects occurring simultaneously here. As the contact conductance drops the achieved temperature will increase and radiative losses scale as T^4, and thus the lower emissivity of the flat-flat case becomes more dominate, and leads to higher temperatures.

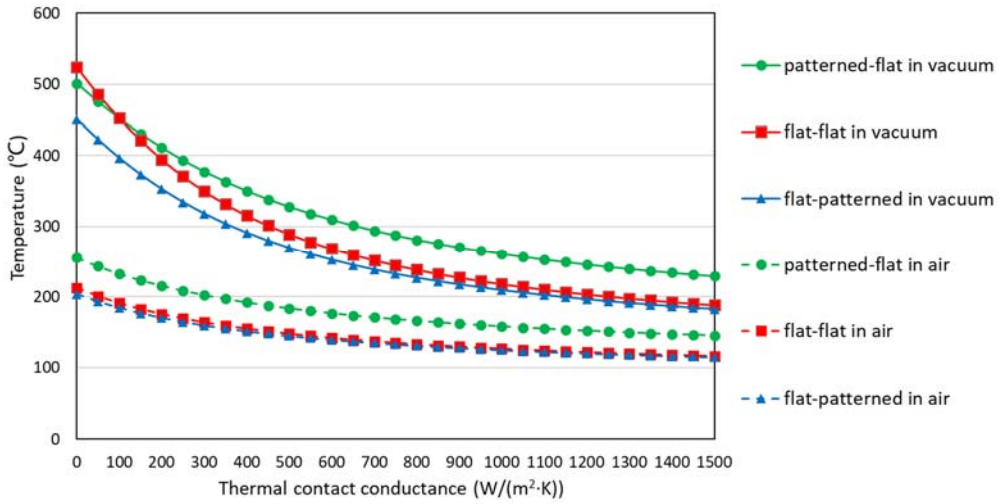

Figure 13 **:** COMSOL simulation of the effects on the highest achieved temperatures by varying the thermal contact conductance between the molybdenum sample and the quartz

Thermal Measurement

Measurements were then undertaken and shown in Fig. 14 for three cases in air and in vacuum. The pressure inside the vacuum chamber is controlled at around 0.15 Torr

for the vacuum cases. We used $700\ W/(m^2 \cdot K)$ for the thermal contact conductance in the simulation which resulted in good agreement with the measurements.

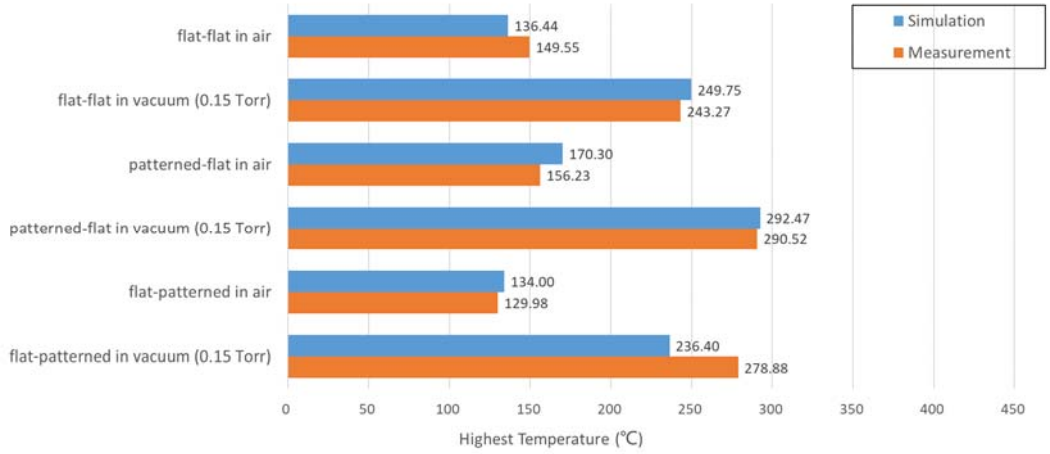

Figure 14 : COMSOL simulated (thermal contact conductance=$\boldsymbol{700\ W/(m^2 \cdot K)}$) and measured highest achieved temperature of patterned-flat, flat-flat, flat-patterned cases in air and vacuum (0.15 Torr)

Fig. 15 shows a further measurement in a reduced vacuum level of 0.005 Torr compared to the of 0.15 Torr measurement shown in Fig. 14. It can be seen that much higher temperature is now being achieved. In theory, the vacuum level in the chamber has little impact on the temperature when the pressure is under 1 Torr. For example, the highest temperature only drops 2.3% when the pressure increases from 0.001 Torr to 1 Torr in the simulation. However, the 0.005 Torr measurement result has a 48.2% increase compared to the 0.15 Torr one. It is difficult to explain such a result, but we speculate that this might be due to decreased contact conductance between the sample and the quartz in the 0.005 Torr case. When the sample has patterned surface contacting the quartz the thermal contact conductance is lower due to the roughness of the patterned

surface. The flat-patterned case will have less conductive loss compared to the patterned-flat and flat-flat case. Thus in Fig. 15 we have used a thermal contact conductance of $50\,W/(m^2 \cdot K)$ which gives a good level of agreement. This highlights the fact that much higher temperatures can be achieved by minimising the contact heat loss with the design improvement of the sample and the quartz holder.

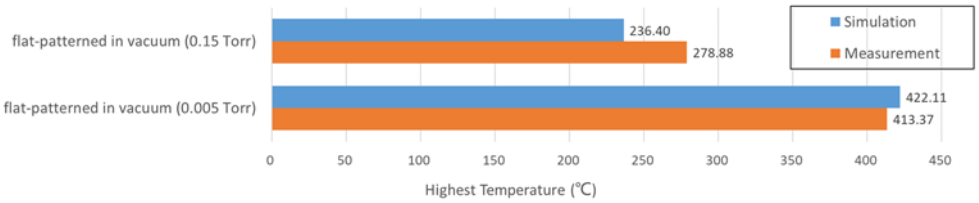

Fig. 15 COMSOL simulated (thermal contact conductance=$\boldsymbol{700\ W/(m^2 \cdot K)}$ for 0.15 Torr and $\boldsymbol{50\ W/(m^2 \cdot K)}$ for 0.005 Torr) and measured highest achieved temperature of flat-patterned case in vacuum of 0.15 Torr and 0.005 Torr

6. Conclusions

This paper has presented the measured optical absorptivity and emissivity of micro-patterned molybdenum produced by laser etching. We have shown that this technique dramatically increases the absorptivity of molybdenum across 500-900 nm which is ideal for solar thermal applications. Temperature results have been shown for the structures with different hole sizes and different periods in air. COMSOL simulation has been used to predict the maximum temperature achievable in vacuum. We have designed a vacuum device and measured the temperatures achieved by patterned and unpatterned molybdenum samples in air and in vacuum. It shows that more than $400\ ℃$ can be achieved with a solar simulator. In addition, our results provide evidence for the

importance of minimising the emissivity of the patterned surface at high temperatures >400 ℃. In future work, we aim to further reduce the contacting area between the sample and the quartz and introduce a cold cathode into a fully sealed commercial grade vacuum device. Surface treatment of the molybdenum will be used to maximise the thermionic emission [5].

Acknowledgements

The Authors would like to acknowledge John Rowden for the help on the construction of the vacuum chamber. This research is funded by the EPSRC under "Beta-enhanced thermionic energy converters and nuclear batteries employing nanostructured diamond electrodes" (EP/K030302/1)

References

1. Kalogirou, S.A., *Solar thermal collectors and applications.* Progress in Energy and Combustion Science, 2004. **30**(3): p. 231-295.
2. Naito, H., et al., *Development of a solar receiver for a high-efficiency thermionic/thermoelectric conversion system.* Solar Energy, 1996. **58**(4): p. 191-195.
3. Atkinson, C., et al., *Coatings for concentrating solar systems–A review.* Renewable and Sustainable Energy Reviews, 2015. **45**: p. 113-122.
4. Bermel, P., et al., *Selective solar absorbers.* Annual Review of Heat Transfer, 2012. **15**.

5. Dominguez-Andrade, H., et al., *Characterisation of thermionic emission current with a laser-heated system.* Review of Scientific Instruments, 2019. **90**(4): p. 045110.

6. Nunez-Sanchez, S., et al., *Molybdenum gratings as a high-temperature refractory platform for plasmonic heat generators in the infrared.* Micro & Nano Letters, 2018. **13**(9): p. 1325-1328.

7. Solak, H.H., C. Dais, and F. Clube, *Displacement Talbot lithography: a new method for high-resolution patterning of large areas.* Optics express, 2011. **19**(11): p. 10686-10691.

8. Carr, D.W. and R.C. Tiberio, *Direct-write electron beam lithography: History and state of the art.* MRS Online Proceedings Library Archive, 1999. **584**.

9. Chou, S.Y., P.R. Krauss, and P.J. Renstrom, *Imprint lithography with 25-nanometer resolution.* Science, 1996. **272**(5258): p. 85-87.

10. van Wolferen, H. and L. Abelmann, *Laser interference lithography.* Lithography: Principles, processes and materials, 2011: p. 133-148.

11. Ahmad, N., et al., *Ultra-thin metal films for enhanced solar absorption.* Nano Energy, 2012. **1**(6): p. 777-782.

12. Ahmad, N., J. Stokes, and M.J. Cryan, *Solar absorbers using 1D and 2D periodic nanostructured nickel films.* Journal of Optics, 2014. **16**(12): p. 125003.

13. Wan, C., L. Chen, and M.J. Cryan, *Broadband metasurface absorber for solar thermal applications.* Journal of Optics, 2015. **17**(12): p. 125103.

14. Wan, C., et al., *A selective metasurface absorber with an amorphous carbon interlayer for solar thermal applications.* Nano Energy, 2016. **26**: p. 392-397.

15. Molesky, S., C.J. Dewalt, and Z. Jacob, *High temperature epsilon-near-zero and epsilon-near-pole metamaterial emitters for thermophotovoltaics.* Optics express, 2013. **21**(101): p. A96-A110.

16. Guo, Y., et al., *Thermal excitation of plasmons for near-field thermophotovoltaics.* Applied Physics Letters, 2014. **105**(7): p. 073903.

17. Klotzbach, U., et al., *Laser micromachining*, in *Fabrication and Characterization in the Micro-Nano Range*. 2011, Springer. p. 29-46.

18. Pham, D.T., S.S. Dimov, and P.V. Petkov, *Laser milling of ceramic components.* International Journal of Machine Tools and Manufacture, 2007. **47**(3-4): p. 618-626.

19. Multiphysics, C., *Introduction to COMSOL Multiphysics®.* COMSOL Multiphysics, Burlington, MA, accessed Feb, 1998. **9**: p. 2018.

20. Churchill, S.W. and H.H.S. Chu, *Correlating equations for laminar and turbulent free convection from a vertical plate.* International journal of heat and mass transfer, 1975. **18**(11): p. 1323-1329.

21. McAdams, W.H., *Heat Transmission,(1954).* McGraw Hills, 2012.

22. Data, S.I. and C.O. Power, *ORIEL PRODUCT TRAINING.*

23. *A. Croot, G. Wan, A. Rowan, H. D. Andrade, J. A. Smith and N. A. Fox, "Beta radiation enhanced Thermionic emission from Diamond Thin Films", Frontiers in Mechanical Engineering November 2017 | Volume 3 | Article 17*

24. Palik, E.D., *Handbook of optical constants of solids*. Vol. 3. 1998: Academic press.

25. D.K. De et al, “Highly Improved Thermionic Energy Converter”, Journal of Physics: Conference Series Volume 1378, Issue 2, 18 December 2019, Article number 022001